

The Widespread Presence of Nanometer-size Dust Grains in the Interstellar Medium of Galaxies

Yanxia Xie¹, Luis C. Ho^{1,2}, Aigen Li³, and Jinyi Shangguan^{1,2}

ABSTRACT

Interstellar dust spans a wide range in size distribution, ranging from ultra-small grains of a few Ångströms to micronmeter-size grains. While the presence of nanometer-size dust grains in the Galactic interstellar medium was speculated six decades ago and was previously suggested based on early infrared observations, systematic and direct analysis of their properties over a wide range of environments has been lacking. Here we report the detection of nanometer-size dust grains that appear to be universally present in a wide variety of astronomical environments, from Galactic high-latitude clouds to nearby star-forming galaxies and galaxies with low levels of nuclear activity. The prevalence of such a grain population is revealed conclusively as prominent mid-infrared continuum emission at $\lambda \lesssim 10 \mu\text{m}$ seen in the *Spitzer*/IRS data, characterized by temperatures of $\sim 300\text{--}400 \text{ K}$ that are significantly higher than the equilibrium temperatures of common, submicron-size grains in typical galactic environments. We propose that the optimal carriers of this pervasive, featureless hot dust component are very small carbonaceous (e.g., graphite) grains of nanometer size that are transiently heated by single-photon absorption. This grain population accounts for $\sim 1.4\%$ of the total infrared emission at $\sim 5\text{--}3000 \mu\text{m}$ and $\sim 0.4\%$ of the total interstellar dust mass.

Subject headings: dust, extinction — infrared: ISM — infrared: galaxies — radiation mechanisms: non-thermal

¹Kavli Institute for Astronomy and Astrophysics, Peking University, Beijing 100871, China; yanxia.xie@pku.edu.cn, lho.pku@gmail.com

²Department of Astronomy, School of Physics, Peking University, Beijing 100871, China; shangguan@pku.edu.cn

³Department of Physics and Astronomy, University of Missouri, Columbia, MO 65211, USA; lia@missouri.edu

1. Introduction

The concept of very small ($\sim 10 \text{ \AA}$) dust grains was first put forward to account for interstellar reddening (Platt 1956). It was later realized that these grains are small enough that their time-averaged heat capacities are comparable to or smaller than the energy of a single photon that heats the grains (Greenberg 1968). Theoretical calculations predict that the temperature of ultrasmall grains suffers large fluctuations and can be stochastically heated by absorbing a single photon to reach instantaneously several hundred Kelvin, considerably higher than the equilibrium temperature of $\sim 15\text{--}30 \text{ K}$ reached with the radiation field for submicron grains (Duley 1973; Greenberg & Hong 1974; Purcell 1976; Andriesse 1978; Draine & Anderson 1985). Exposed to starlight of different levels of intensity (e.g., at different distances from the star), stochastically heated nanometer-size grains emit in the infrared (IR) essentially with the same spectral profile characterized by the same temperature (Sellgren 1984; Draine & Li 2001).

Sporadic evidence for the existence of very small grains came from early observations of Galactic and extragalactic sources. The first detection was reported in the H II region M 17 S, which showed very similar source profiles in the IR characterized by a temperature of $\sim 150 \text{ K}$, independent of the distance from the heating star (Andriesse & Vries 1976). Similarly, in three visual reflection nebulae, a uniform near-IR continuum emission at $\sim 2\text{--}5 \mu\text{m}$ was detected to have a color temperature of $\sim 800\text{--}1000 \text{ K}$, again independent of distance from the star (Sellgren et al. 1983). Two of these three reflection nebulae, as well as many other environments, also exhibit a broad, featureless band at $\sim 5400\text{--}9500 \text{ \AA}$, known as the “extended red emission”, generally attributed to photoluminescence by nanoparticles (Witt 2000). A constant continuum emission between $\sim 3\text{--}5 \mu\text{m}$ has been detected in star-forming galaxies based on spectroscopic observations from the *Infrared Space Observatory* (ISO); it appears to depend very weakly on the galaxy parameters and far-IR colors (Helou et al. 2000; Sturm et al. 2000; Lu et al. 2003). Evidence for small grains in the Galactic diffuse interstellar medium (ISM) is also revealed as excess emission from IR cirrus observed at 12 and $25 \mu\text{m}$ by the *Infrared Astronomical Satellite* (IRAS; Boulanger & Perault 1988) and at 3.5, 4.9, 12 and $25 \mu\text{m}$ by the Diffuse Infrared Background Experiment (DIRBE) on board the *Cosmic Background Explorer* (COBE; Arendt et al. 1998). Furthermore, the steeply rising far-UV extinction at $\lambda^{-1} > 6 \mu\text{m}^{-1}$ (see Li 2004a) and the “anomalous microwave emission”, an important Galactic foreground of the cosmic microwave background radiation in the $\sim 10\text{--}100 \text{ GHz}$ region, suggest that the ISM contains a considerable amount of small grains (see Draine & Lazarian 1998, Hensley & Draine 2017a).

In this work we report the detection of hot ($\sim 300\text{--}400 \text{ K}$) continuum emission, which we attribute to nanometer-size dust grains, over a wide range of Galactic and extragalactic

environments. This component of the ISM, long hypothesized from models and implied in early observations, is here detected unambiguously in modern high-quality mid-IR spectra (see §2). We propose that nanometer-size carbonaceous grains, transiently heated by single-photon absorption, are optimal carriers for this hot dust component (see §3.1 and §3.2). We show that nanometer-size grains lock up $\sim 1.5\%$ of the carbon and $\sim 0.4\%$ of the total interstellar dust mass (see §3.3).

2. Observational Material and Method of Analysis

The data analyzed in this work are based on mid-IR spectra taken with the Infrared Spectrograph (IRS; Houck et al. 2004) onboard the *Spitzer Space Telescope* (Werner et al. 2004). The IRS has both a low-resolution and a high-resolution mode. We focus on the low-resolution spectra, whose broader spectral coverage provides a better probe of the hot continuum emission. The short-low mode has a slit size of $3.7'' \times 57''$ and $3.6'' \times 57''$, covering, respectively, $\sim 7.4\text{--}14.5\ \mu\text{m}$ and $\sim 5.2\text{--}7.7\ \mu\text{m}$. The long-low mode has a slit size of $10.7'' \times 168''$ and $10.5'' \times 168''$, covering, respectively, $\sim 19.5\text{--}38.0\ \mu\text{m}$ and $\sim 14.0\text{--}21.3\ \mu\text{m}$. The resolution varies from ~ 64 to ~ 128 in each segment. We use the spectra of high signal-to-noise ratio from the *Spitzer Infrared Nearby Galaxy Survey* (SINGS¹; Kennicutt et al. 2003, Smith et al. 2007), focusing on a sample of 46 objects, comprising 24 star-forming (H II) galaxies and 22 galaxies with relatively low-luminosity active galactic nuclei, including 14 low-ionization nuclear emission-line regions (LINERs) and eight Seyferts (Ho 2008). In addition to the galaxy sample, we also choose the IRS low-resolution spectra taken at four different positions (A–D) within the Galactic HLC DCld 300.2–16.9 (Ingalls et al. 2011), which lies at a distance of 70 ± 15 pc from the solar neighborhood.

The mid-IR spectra of the ISM in our Galaxy and in external galaxies exhibit a plethora of emission components from dust and gas. Apart from the prominent polycyclic aromatic hydrocarbon (PAH) features located at 6.2, 7.7, 8.6, and $11.3\ \mu\text{m}$, the mid-IR region also captures dust continuum emission of various temperatures arising from grains of different sizes, as well as a wealth of ionic and molecular gas emission lines. The detailed elaboration over the characteristics of the mid-IR spectra is presented in a companion paper (Xie et al. 2018), which presents a new methodology to decompose the different spectral components. Here we summarize the main steps of spectral decomposition.

To reduce the complexity and potential contamination from many overlapping compo-

¹The reduced data are taken from the SINGS Legacy Survey web site <http://irsa.ipac.caltech.edu/data/SPITZER/SINGS/>.

nents of the mid-IR spectra, we begin by first removing the ionic and molecular lines that are not blended with PAH features. We describe the PAH emission using a theoretical PAH spectrum calculated adopting a starlight intensity $U=1$ times of the interstellar radiation field (ISRF) of the solar neighborhood ISM (Mathis et al. 1983; hereafter MMP83) and grain sizes $3.5 \text{ \AA} < a < 20 \text{ \AA}$. The PAH spectrum is relatively insensitive to radiation intensities ranging up to $U \approx 10^4$. To account for the dust continuum emission, we adopt a linear combination of three modified blackbodies (i.e., graybodies) of different temperatures (“hot”, “warm”, and “cold”).² All four components are subject to extinction by dust. In all, the rest-frame spectrum is fit through χ^2 minimization to the following model spectrum:

$$F_\nu = [A^{\text{PAH}} J_\nu^{\text{PAH}} + A^h B_\nu(T^h)/\lambda^\beta + A^w B_\nu(T^w)/\lambda^\beta + A^c B_\nu(T^c)/\lambda^\beta] \exp(-A_\lambda/1.086), \quad (1)$$

where A^{PAH} is the scale factor of the PAH template J_ν^{PAH} ; A^h , A^w , and A^c are, respectively, the amplitudes of the hot, warm, and cold dust components represented as modified blackbodies of temperature T^h , T^w , and T^c ; $B_\nu(T)$ is the Planck function of temperature T at frequency ν ; β is the dust emissivity index, assumed the same (Li 2009) for all three modified blackbodies and fixed to 2;³ and A_λ is the extinction, adopted from the theoretical curve of (Wang et al. 2015). We obtain the best fit for each galaxy using the IDL code **MPFIT**, a χ^2 -minimization routine based on the Levenberg-Marquardt algorithm (Markwardt 2009). The error of each parameter is estimated based on Monte Carlo simulations (Xie et al. 2018). Table 1 list the derived temperatures and errors of each component for the sample.

3. Results and Discussions

In Figure 1, we illustrate the decomposition of the mid-IR spectra of a Galactic high-latitude cloud (HLC), a normal star-forming galaxy, and a low-luminosity active galaxy.

²By “hot”, “warm,” and “cold,” we merely refer to the different dust components adopted in our methodology to account for the continuum emission at $\sim 5\text{--}40 \mu\text{m}$ underlying the PAH emission features; they differ from the conventional terminology for dust temperatures in galaxies (Li 2004b). For example, the conventional terminology defines cold dust as submicron-size dust of equilibrium temperatures $\sim 15\text{--}30 \text{ K}$, which dominates the emission at $\lambda \gtrsim 100 \mu\text{m}$, while the cold component defined here is much warmer ($\sim 40\text{--}70 \text{ K}$).

³Assuming that all dust particles are spherical and are composed of electrons and ions, they can be treated as a sum of dipoles of classical Lorentz harmonic oscillators, oscillating under the force of an electromagnetic field. For submicron-sized (and smaller) grains that satisfy the Rayleigh limit in the IR ($2\pi a/\lambda \ll 1$), the absorption by dust of incident radiation can be approximated as $\sim \lambda^{-2}$ (i.e., $\beta \approx 2$), in accordance with the solution for the motion of harmonic oscillators, where λ is the wavelength of the incident electromagnetic wave. In practical situations, β may vary from ~ 1.5 to ~ 2 , which indicates that the vibration of the dust grain deviates from that of ideal harmonic oscillation (see Draine 2003 and Li 2009 for more details). The determination of the exact value of β requires full information on the IR SED. In this work, we fix β to 2.

Both classes of objects under investigation—Galactic HLCs and nearby galaxies—exhibit a prominent mid-IR continuum consistent with thermal radiation from very hot dust grains. The temperatures span a relatively narrow range, from ~ 300 to ~ 400 K (Figure 2, blue histogram). Not only are the temperatures high, the most surprising aspect is that they are relatively uniform across extremely diverse environments, from Galactic HLCs to local star-forming galaxies and active galaxies of different types, from LINERs to Seyferts, which cover a range of ionization levels and black hole accretion rates (Ho 2008, 2009).

The derived temperatures are very robust against the details of the spectral decomposition. Our companion paper (Xie et al. 2018) shows that for grain sizes $a \lesssim 20$ Å or $a \lesssim 50$ Å, the PAH spectrum for $\lambda \lesssim 15$ μm is quite uniform for a wide range of photon densities from $U = 1$ to $U = 10^6$ (see Figure 2 in Xie et al. 2018), and that the derived PAH and dust temperatures also vary little among fits adopting PAH templates with $U \lesssim 10^4$ (see Figure 12 in Xie et al. 2018). To ascertain the robustness of the derived dust temperatures, we also consider an alternate empirical PAH template derived from the “Continuum And Feature Extraction” (CAFE) method of Marshall et al. (2007) and repeat the fits. We find that the derived dust temperature distributions remain virtually unchanged relative to those derived from our theoretical PAH template (see Figure 2). Also, the derived hot dust temperature is relatively insensitive to the omission of longer wavelength data extending to the far-IR (see Xie et al. 2018). Given the pervasiveness of the hot-dust component, why has it gone largely unnoticed? The reason, we suspect, stems from the sheer complexity of the mid-IR spectra, especially the overwhelming dominance of the many strong, overlapping PAH features, whose broad and extended line profiles effectively mask the local continuum. Absent an effective, physically well-motivated method to decouple the PAH spectrum, the underlying mid-IR continuum becomes difficult to disentangle. In §3.1, we discuss in more detail the difference between PAHs and the emitter of the hot continuum derived here.

The equilibrium temperature of dust depends on the strength of the radiation field to which it is exposed, as $T \propto U^{1/(4+\beta)}$, where U describes the starlight intensity that heats the grains and β is the power-law index of dust emissivity in the far-IR, assumed $\lambda^{-\beta}$, with $\beta \approx 1.5 - 2$ for greybody emission. The above scaling relation indicates that an increase of starlight intensity by a factor of 100 only induces a temperature rise of a factor of ~ 2 . Accumulating evidence shows that the dust temperature in the ISM, both near and far, occupies a very narrow range. For instance, the emission of the diffuse interstellar dust of the Milky Way, with an average star formation rate of $\sim 1.7 M_{\odot} \text{ yr}^{-1}$ (Licquia & Newman 2015), peaks at ~ 18 K (Planck Collaboration 2011). Extensive *Herschel* surveys of local star-forming and starburst galaxies reveal that the bulk of the ISM mass has temperatures $T \approx 15\text{--}30$ K (Dunne et al. 2011; Auld et al. 2013). High-redshift ($z \approx 1.4\text{--}3$) submillimeter galaxies also display a narrow range of dust temperatures (Scoville et al. 2014). The narrow

temperature distribution for the bulk of the ISM, at both low and high redshifts, indicates that the interstellar radiation field of normal star-forming or starburst galaxies does not vary significantly. Indeed, the IR spectral energy distribution (SED) of the SINGS galaxies all peak around $100\ \mu\text{m}$, corresponding to dust temperature of $\sim 20\text{--}30\ \text{K}$ (Dale et al. 2012).

If the observed hot dust emission described in this work is ascribed to an equilibrium temperature, it would require a dust-heating starlight intensity a few million times higher than that found in typical star-forming galaxies. In principle, this can be achieved from intense starburst activity confined to a sufficiently compact region. However, such a scenario is utterly implausible for HLCs, which have no ongoing embedded star formation and are located far from the Galactic disk ($70 \pm 15\ \text{pc}$). If the observed mid-IR emission of the HLC DCld 300.2–16.9 is from equilibrium dust radiation from external heating, there should be a temperature gradient across the cloud varying with distance from the Galactic disk. No such trend is seen. As for the H II galaxies considered here, they have modest integrated star formation rates of $\lesssim 1\ M_\odot\ \text{yr}^{-1}$ to $\sim 15\ M_\odot\ \text{yr}^{-1}$, distributed broadly across the entire disk. The IRS slit only captures a portion of the star formation from the central kpc, which does not contribute a significant amount of heating photons. The same can be said of the active galaxies in our sample. While technically classified as accretion-powered sources, the level of nuclear activity in these nearby LINERs and Seyferts is incredibly feeble (Ho 2008, 2009). It is impossible for these low-luminosity AGNs to provide the radiation intensity to heat the dust grains to the requisite high temperatures. Furthermore, if the observed high temperature is generated from hot, optically thin dust heated by intense UV photons, we would expect to see silicate emission at ~ 10 and $18\ \mu\text{m}$. None of the objects in our sample shows silicate emission; some exhibit, at most, mild silicate absorption. Therefore, equilibrium heating can be ruled out as the emission mechanism for the strikingly high temperatures observed in the mid-IR continuum.

We suggest that the ubiquitous presence of high-temperature dust originates from nano grains heated by single-photon absorption (i.e., stochastic heating), in the manner first proposed 35 years ago (Sellgren et al. 1983, Sellgren 1984; Weiland et al. 1986). The temperature attained through stochastic heating scales only with the grain size and the average photon energy and is independent of the distance from the heating source. Such a mechanism provides a natural explanation for the relatively invariant mid-IR continuum emission detected toward sources as diverse as Galactic HLCs and low-luminosity active galaxies. The grain size corresponding to this emission is $\lesssim 1\ \text{nm}$ (see § 3.1).

3.1. Grain Size

Upon absorption of a photon of energy $h\nu$, a grain undergoing single-photon heating will be very quickly ($< 10^{-3}$ s) heated to its peak temperature T_{peak} and then rapidly cools down in a few seconds by emitting most of the absorbed energy at T_{peak} (see Draine & Li 2001). The peak temperature is determined from

$$\int_0^{T_{\text{peak}}} C(T) dT = h\nu , \quad (2)$$

where $C(T)$ is the specific heat of the grain at temperature T , h is the Planck constant, and ν is the frequency of the absorbed photon. Let T_{D} be the Debye temperature of the grain material (e.g., $T_{\text{D}} \approx 420$ K for graphite, $T_{\text{D}} \approx 542$ K for quartz SiO_2 ; see Draine & Li 2001) and $N_{\text{atom}} \propto a^3$ be the number of atoms in a grain of size a . For $T \ll T_{\text{D}}$,

$$\frac{C(T)}{N_{\text{atom}}} = \frac{12k\pi^4}{5} \left(\frac{T}{T_{\text{D}}} \right)^3 , \quad (3)$$

and therefore,

$$T_{\text{peak}} = \left(\frac{5}{3k\pi^4} \right)^{1/4} (h\nu)^{1/4} N_{\text{atom}}^{-1/4} T_{\text{D}}^{3/4} \propto a^{-3/4} (h\nu)^{1/4} . \quad (4)$$

For $T \gg T_{\text{D}}$, $C(T) \approx 3N_{\text{atom}} k$ (i.e., the Dulong-Petit law), where k is the Boltzman constant, and therefore T_{peak} will be appreciably higher than that given by eq. 4, but it is always true that $T_{\text{peak}} \propto a^{-3/4} (h\nu)^{1/4}$.

We can estimate the size of the ultrasmall grains responsible for the hot ($T^h \approx 300 - 400$ K) component from eq. 2. We take $T_{\text{peak}} \approx T^h$ because grains heated by single photons radiate most of their energy at T_{peak} (Draine & Li 2001). Since T_{peak} is comparable to T_{D} , we cannot simply use eq. 3 for $C(T)$ which is valid for $T \ll T_{\text{D}}$. Following Draine & Li (2001), we will approximate the specific heats of graphite and silicate materials in terms of the following Debye models⁴:

$$C_{\text{gra}}(T) = (N_{\text{atom}} - 2)k \left[f'_2 \left(\frac{T}{863 \text{ K}} \right) + 2 f'_2 \left(\frac{T}{2504 \text{ K}} \right) \right] , \quad (5)$$

$$C_{\text{sil}}(T) = (N_{\text{atom}} - 2)k \left[2f'_2 \left(\frac{T}{500 \text{ K}} \right) + f'_3 \left(\frac{T}{1500 \text{ K}} \right) \right] , \quad (6)$$

⁴There is a typographical error in the expression of $f_n(x)$ in eq. 10 of Draine & Li (2001).

$$f_n(x) \equiv n \int_0^1 \frac{y^n dy}{\exp(y/x) - 1} \quad , \quad f'_n(x) \equiv \frac{d}{dx} f_n(x) \quad . \quad (7)$$

For the photon energy $h\nu$, we consider the *mean* photon energy $\langle h\nu \rangle$ that an ultrasmall grain would absorb when exposed to starlight of radiation density u_ν (or radiation intensity $cu_\nu/4\pi$, where c is the speed of light):

$$\langle h\nu \rangle = \frac{\int C_{\text{abs}}(a, \nu) cu_\nu d\nu}{\int C_{\text{abs}}(a, \nu) cu_\nu / h\nu d\nu} \quad , \quad (8)$$

where $C_{\text{abs}}(a, \nu)$ is the absorption cross section of the grain of size a at frequency ν . If we approximate the radiation field of normal star-forming galaxies by the MMP83 ISRF of the solar neighborhood (Mathis et al. 1983), we obtain $\langle h\nu \rangle \approx 7.5$ eV for nanometer-size silicate grains and $\langle h\nu \rangle \approx 3.5$ eV for nanometer-size graphitic grains. Similarly, for starburst galaxies, if we approximate their radiation field by the UV, visible, and near-IR spectrum of NGC 7714 (Brown et al. 2014), we estimate $\langle h\nu \rangle \approx 8.8$ eV for nanometer-size silicate grains and $\langle h\nu \rangle \approx 4.8$ eV for nanometer-size graphitic grains. The mean photon energy absorbed by nanometer-size grains is insensitive to grain size because such small grains, even in the UV, are in the Rayleigh regime and thus $C_{\text{abs}}(a, \nu)/a^3$ is independent of a .

With $\langle h\nu \rangle \approx 7.5$ eV and 8.8 eV, we derive, respectively, $a \approx 8.0 \pm 0.6$ Å and 8.5 ± 0.7 Å for silicate grains of $T_{\text{peak}} \approx 300 - 400$ K. Similarly, with $\langle h\nu \rangle \approx 3.5$ eV and 4.8 eV, we derive $a \approx 7.7 \pm 0.8$ Å and 8.4 ± 0.9 Å for graphitic grains of $T_{\text{peak}} \approx 300 - 400$ K. We will call these ultrasmall grains (which are responsible for the mid-IR continuum at $\lambda \lesssim 10$ μm) “nanometer-size” grains. These nano grains differ from the so-called “very small grains” (VSGs) reported by Sellgren et al. (1983) and Sturm et al. (2000) that emit at $\sim 3-5$ μm. The latter are smaller in size, as they should be transiently heated to a higher peak temperature (i.e., $T_{\text{peak}} \gtrsim 800$ K). These nano grains are also distinct from the VSG component invoked by grain models in the post-*IRAS* era (e.g., see Désert et al. 1990; Siebenmorgen & Kruegel 1992; Dwek et al. 1997; Li & Greenberg 1997; Zubko et al. 2004; Compiegne et al. 2011). The nanometer-size component inferred here emits mostly at $\lambda \lesssim 10$ μm and negligibly at $\lambda \gtrsim 20$ μm, while the VSGs invoked by the aforementioned models are much larger in size and dominate the *IRAS* 25 μm emission and in part the *IRAS* 60 μm emission. Also, the nano component discussed here differs from the VSG component of Boissel et al. (2001) and Rapacioli et al. (2005) derived from the singular value decomposition method coupled with a Monte Carlo search algorithm. The latter is essentially a PAH cluster and exhibits a broad band at ~ 7.8 μm, while the nano component discussed here emits a smooth continuum.

The nanometer-size grains inferred here are also different from PAHs. The so-called “unidentified IR emission” (UIE) bands at 3.3, 6.2, 7.7, 8.6, and 11.3 μm commonly seen in various astronomical environments have been attributed to tiny carbonaceous grains or

very large molecules of size $a < 50 \text{ \AA}$ and carbon atoms $N_C < 2 \times 10^4$ (e.g., see Figure 7 of Draine & Li 2007), with PAH molecules as the mostly likely carrier (Léger & Puget 1984; Allamandola et al. 1985). PAHs emit remarkably similarly in objects spanning several orders of magnitude in radiation density (e.g., Boulanger et al. 2000). Xie et al. (2018) show that PAH spectra barely change in environments as diverse as Galactic HLCs, nearby star-forming and starburst galaxies, and even in galaxies hosting AGNs of both low and high luminosity. The grains (or large molecules) contributing to the PAH emission features have similar nature to grains responsible for the uniform hot continuum emission: both are excited by stochastic heating from single-photon absorption (Draine & Li 2001, 2007). However, experimentally, gas-phase, free-flying PAH molecules of several tens of carbon atoms do not show strong continuum opacity at $\sim 1\text{--}5 \mu\text{m}$ (see Bauschlicher et al. 2018 and references therein). Also, An & Sellgren (2003) found that in NGC 2023, a prototypical reflection nebula, the $3.3 \mu\text{m}$ PAH emission and the underlying continuum emission at $\sim 2 \mu\text{m}$ are spatially separated, suggesting that PAHs are not the carrier of the $2 \mu\text{m}$ continuum emission.⁵ Alternatively, Kwok & Zhang (2011) suggest that organic nanoparticles with a mixed aromatic-aliphatic structure could be responsible for *both* the PAH emission bands *and* the underlying continuum. Future spatially resolved observations (e.g., *JWST*) that can map the two components will provide new insight into their physical separations and chemical carriers.

3.2. Chemical Carrier

Using the technique of Draine & Li (2001) developed for modeling the vibrational excitation of stochastically heated ultrasmall grains, we calculate the IR emissivity of spherical nanometer-size grains of different chemical compositions of radii $a = 5, 7.5, 10$, and 15 \AA , respectively. We consider silicate and graphite grains. We consider a heating source similar to that of the MMP83 solar neighborhood ISRF (“MMP83-type ISRF”; Mathis et al. 1983)

⁵Kahanpää et al. (2003) correlated the total PAH emission (I_{PAH}) at $\sim 5.8\text{--}11.6 \mu\text{m}$ with the *IRAS* 12 and $100 \mu\text{m}$ surface brightness (I_{12}, I_{100}) measured across the Galaxy. They found that I_{PAH} correlates with I_{12} and I_{100} fairly well. While a close correlation between I_{PAH} and I_{12} is expected since the *IRAS* $12 \mu\text{m}$ emission is predominantly contributed by PAHs (e.g., see Figure 8 of Li & Draine 2001), the correlation between I_{PAH} and I_{100} does not necessarily mean that PAHs and the grains responsible for the $100 \mu\text{m}$ continuum emission are physically associated. The latter correlation could merely reflect the fact that both PAHs and the submicron-size grains — the dominant emitter of the $100 \mu\text{m}$ thermal continuum — correlate with the total amount of interstellar material (e.g., the hydrogen column density N_{H}). In order to properly examine whether PAHs and the carriers of the $100 \mu\text{m}$ emission are indeed physically related, one needs to eliminate their common correlations with N_{H} , by comparing $I_{\text{PAH}}/N_{\text{H}}$ with I_{100}/N_{H} .

and a harder, more intense starburst ISRF (approximated by the UV, visible and near-IR spectrum of NGC 7714; Brown et al. 2014) with $U = 100$ (“starburst-type ISRF”). As illustrated in Figure 3, nanometer-size silicate grains emit prominent features at $9.7\ \mu\text{m}$ (Si–O) and $18\ \mu\text{m}$ (O–Si–O), whether the ISRF is MMP83-type or starburst-type (see Figure 3a, c). These are not seen in any of the sources discussed in this work. Therefore, we can exclude nanometer-size amorphous silicates as the main carrier of the hot dust emission observed in the mid-IR. In contrast, the free electrons of nanometer-size graphitic grains emit a smooth continuum in the mid-IR (see Figure 3b, d). The lack of any prominent spectral features from nano graphite is consistent with the “derived” featureless hot component emission.

At a first glance, nanometer-size amorphous carbon (AC) grains could also be a plausible carrier for the hot component, for they also emit a featureless continuum in the mid-IR. In the diffuse ISM, however, AC grains are likely hydrogenated, as revealed by the $3.4\ \mu\text{m}$ aliphatic C–H stretch *absorption* band (Pendleton & Allamandola 2002). If nanometer-size AC grains are present in the ISM, e.g., resulting from the collisional fragmentation of bulk, submicron-size hydrogenated amorphous carbon (HAC) grains, unless they are completely dehydrogenated, they would emit at $3.4\ \mu\text{m}$ because of single-photon heating. Observationally, the $3.4\ \mu\text{m}$ aliphatic C–H *emission* feature is mostly seen in cool, UV-poor reflection nebulae and proto-planetary nebulae and is often much weaker than the $3.3\ \mu\text{m}$ aromatic C–H band (Yang et al. 2013). Therefore, it is less likely that the nanometer-size component inferred here is from nanometer-size AC grains unless their H atoms are completely knocked off.

Like graphite, nanometer-size iron grains also emit a featureless continuum in the IR. While they seem to be stable against sublimation in the ISM (Hensley & Draine 2017b) and have recently been invoked by to account for the “anomalous microwave emission” (Hensley & Draine 2017a), it is not clear if they could survive against oxidation (Jones 1990). Nanometer-size iron oxides would exhibit several spectral features, e.g., FeO at $\sim 21\ \mu\text{m}$, Fe₂O₃ at $\sim 20.5\ \mu\text{m}$ and $27.5\ \mu\text{m}$, and Fe₃O₄ at $\sim 16.5\ \mu\text{m}$ and $24\ \mu\text{m}$ (Henning & Mutschke 1997; Koike et al. 2017). However, these features are not seen in the ISM.

In principle, the spectral profile of the hot component should allow us to constrain the composition of the nanometer-size grain population. We do not do so quantitatively because the approach adopted here to determine the spectral shape of the hot component was simplified (see eq. 1), and the actual emission spectrum of a nanometer-size grain is considerably wider than that approximated by a single temperature (Draine & Li 2001). Therefore, it would be an over-interpretation to employ the emission spectrum of the hot component to infer the nanometer-size grain composition (and size distribution). Nevertheless, we propose that nano graphite is primarily responsible for this radiation component, as nanometer-

size graphitic grains emit a smooth continuum in the mid-IR caused by the free electrons of graphite, a semi-metal, and carbon is an abundant element, much more abundant than iron. Presolar graphite grains have been identified in primitive meteorites through isotope anomaly. Nanometer-size graphite grains are a natural product of shock-induced shattering of large, submicron-size graphite grains, or thermal processing of nanodiamonds (Andersson et al. 1998) which are also abundant in primitive meteorites (Lewis et al. 1987). Presolar nanodiamonds are abundant in primitive meteorites and the detection of nanodiamonds through their characteristic emission features at 3.43 and 3.53 μm have been reported in HD 97048 and Elias 1, two Herbig Ae/Be stars, and in HR 4049, a post-asymptotic giant branch star (see Li 2004a and references therein). However, nanodiamonds are unlikely responsible for the hot continuum emission reported in this work since neither the 3.43 μm emission feature nor the 3.53 μm emission feature expected from nanodiamonds is seen in the ISM of the Milky Way and external galaxies.

3.3. Mass Fraction

Let $f_{\text{mass}}(\text{nano})$ be the fraction of the total dust mass in the nanometer-size dust component, $f_{\text{IR}}(\text{nano})$ be the corresponding fraction of the total IR power, $\kappa_{\text{abs}}^{\text{nano}}(\nu)$ be the corresponding mass absorption coefficient, and $\langle \kappa_{\text{abs}}(\nu) \rangle$ be the mean mass absorption coefficient of all dust grains in a galaxy. For energy balance between absorption and emission, we obtain

$$f_{\text{mass}}(\text{nano}) = f_{\text{IR}}(\text{nano}) \frac{\int \langle \kappa_{\text{abs}}(\nu) \rangle c u_{\nu} d\nu}{\int \kappa_{\text{abs}}^{\text{nano}}(\nu) c u_{\nu} d\nu} . \quad (9)$$

This does not involve any dust temperature which is known to be a major source of uncertainties in estimating dust mass. We assume that the bulk dust mixture of the galaxies considered here is more or less the same as that of the Milky Way galaxy (Li & Draine 2001). For the nanometer-size component, we calculate $\kappa_{\text{abs}}^{\text{nano}}(a, \nu) \equiv C_{\text{abs}}(a, \nu)/M$ from graphite grains of $a = 10 \text{ \AA}$, where $M = (4\pi/3) a^3 \rho$ is the mass of a graphite grain of size a and $\rho = 2.24 \text{ g cm}^{-3}$ is the mass density of graphite. Since nanometer-size grains are in the Rayleigh regime from the UV to the far-IR, $\kappa_{\text{abs}}^{\text{nano}}(a, \nu)$ is independent of a .

Estimating $f_{\text{IR}}(\text{nano})$ requires complete coverage of the SED from the near-IR to the far-IR. While sufficient wavelength coverage exists for many of the objects analyzed in this study, the SINGS galaxies are angularly large, and aperture mismatch between the *Spitzer* IRS and *Herschel* observations is a serious problem. Thus, for this portion of the analysis we make use of archival observations from the Great Observatories All-Sky LIRG Survey (GOALS, Armus et al. 2009), a sample of 201 nearby ($z \approx 0.09$) IR-luminous galaxies with complete mid-IR spectra from *Spitzer*/IRS and photometry spanning $\sim 12\text{--}500 \mu\text{m}$ from *IRAS* and

Herschel. We proceed in a stepwise fashion to select a subset of the GOALS objects for which we can compile SEDs that properly sample the same physical scale, despite the vastly different resolutions between the mid-IR and far-IR.

We begin by scaling the flux density of the IRS spectra from the short-low module ($\sim 5.2\text{--}14.5\ \mu\text{m}$; slit width $3.6''$) to match the spectra from the long-low module ($\sim 14.0\text{--}38\ \mu\text{m}$; slit width $10.5''$). We only choose galaxies with sufficiently large distances such that their optical diameters fit within the dimensions of the long-low aperture. As the point-spread function of all the *IRAS* bands comfortably covers the total extent of these galaxies, we require that the IRS $25\ \mu\text{m}$ flux density matches the *IRAS* $25\ \mu\text{m}$ photometry (Sanders et al. 2003), allowing for $\sim 10\%\text{--}15\%$ variation to account for systematic uncertainties between the two datasets. Next, we verified that the *IRAS* 60 and $100\ \mu\text{m}$ photometry closely matches the *Herschel* measurements at 70 and $100\ \mu\text{m}$ (Chu et al. 2017). This ensures that the *Herschel* photometry out to $500\ \mu\text{m}$ can be used. Of the 60 galaxies that match these criteria, we finally select 28 that are starburst-dominated systems according to classifications in the NASA/IPAC Extragalactic Database⁶, the majority of which are based on mid-IR diagnostics (Armus et al. 2007). The IRS spectra of all 28 galaxies exhibit unambiguously strong PAH emission. In Table 2, we present the basic parameters and *Herschel* photometry for this subset of GOALS galaxies.

We fit the complete IR SED using the methodology described in our companion paper Xie et al. (2018), adopting a PAH template for the PAH emission and four modified blackbodies to account for the dust continuum emission (Figure 4). We derive $f_{\text{IR}}(\text{nano})$, the flux fraction radiated from nanometer-size dust, by dividing the integrated hot dust emission with the total radiation from 5 to $3000\ \mu\text{m}$. The results are shown in Figure 5a, where we also plot the flux fraction radiated from PAHs (see Figure 5b). The nanometer-size dust component accounts for $f_{\text{IR}}(\text{nano}) \approx 1.4\%$, independent of the total IR luminosity of the galaxies. PAHs behave similarly, with a median IR power fraction of $\sim 5\%$. An $f_{\text{IR}}(\text{nano})$ of 1.4% translates into $f_{\text{mass}}(\text{nano}) \approx 0.4\%$, for a silicate-graphite mixture like that of the Milky Way diffuse ISM (Weingartner & Draine 2001). This corresponds to a mass fraction of $\sim 1.5\%$ of the total carbon dust, lower than that of PAHs by a factor of ~ 3 .

We note that, in order to account for the $\sim 3\text{--}5\ \mu\text{m}$ continuum emission detected by Sellgren et al. (1983) and Sturm et al. (2000), the astro-PAH model (Li & Draine 2001, Draine & Li 2007) from which the theoretical PAH template was calculated and adopted here incorporates a small amount of “continuum” opacity, equal to $\sim 1\%$ of bulk graphite, although the exact nature of this continuum opacity is unclear. If free-flying PAHs do not

⁶<http://ned.ipac.caltech.edu>

have any continuum opacity in the near IR, the fractional emission contributed by the hot component would be even higher and therefore the quantity of the nanometer-size dust would be larger, and our conclusion of the presence of nanometer-size dust would be even more robust.

The 2175 Å interstellar extinction bump is often attributed to small graphite grains (e.g., see Stecher & Donn 1965; Draine 1988; Mishra & Li 2015, 2017). With such a small mass fraction, the nanometer-size graphite component inferred here from the hot continuum emission at $\lambda \lesssim 10 \mu\text{m}$ cannot be a major contributor to the 2175 Å extinction bump since the latter requires its carrier to lock up $\sim 10\text{--}15\%$ of the total interstellar carbon abundance (Draine 1989).

Lastly, we note that we have not considered high-luminosity active galactic nuclei (e.g., quasars). The mid-IR continuum emission from nanometer-size dust, if present, would be difficult to isolate from the hot dust emission from the nucleus-heated dusty torus (Zhuang et al. 2018). Moreover, stochastic heating is unlikely to be effective in light of the high average photon energy in these luminous systems. As the photon absorption timescale becomes short and comparable to the cooling time, small grains cannot completely cool off in between photon absorption events and hence will eventually attain temperature equilibrium. Large grains can also reach very high temperatures from the frequent absorption of heating photons and peak in the mid-IR (Xie et al. 2017).

4. Summary

We found a hot dust continuum emission at $\lambda \lesssim 10 \mu\text{m}$ of temperature $\sim 300\text{--}400 \text{ K}$ that is widespread in different astronomical environments. This hot continuum component, closely coupled to the PAH emission features, is detected in the mid-IR ($\sim 5\text{--}40 \mu\text{m}$) spectra of Galactic high-latitude clouds, normal star-forming galaxies, and low-luminosity active galaxies. The presence of this hot dust component cannot be explained by equilibrium heating. We propose that the nanometer-size dust grains are transiently heated via single-photon absorption. The most likely carrier are very small (size $\lesssim 10 \text{ Å}$) carbonaceous (e.g., graphitic) grains. They account for $\sim 1.4\%$ of the total IR emission at $\sim 5\text{--}3000 \mu\text{m}$, $\sim 1.5\%$ of the total carbon dust, and $\sim 0.4\%$ of the total dust mass.

We thank the anonymous referee for helpful suggestions which considerably improved the presentation of this paper. This work was supported by the National Key R&D Program of China (2016YFA0400702) and the National Science Foundation of China (11473002, 11721303). Y.X. is supported by China Postdoctoral Science Foundation Grant 2016 M591007.

The Cornell Atlas of *Spitzer*/IRS Sources (CASSIS) is a product of the Infrared Science Center at Cornell University, supported by NASA and JPL.

Table 1. Basic Parameters for the Sample of Galaxies and Galactic High-Latitude Clouds

Source	R.A. (J2000) (hh mm ss.s)	Decl. (J2000) (dd mm ss.s)	Type	Distance (Mpc)	T^h (K)	T^w (K)	T^c (K)
(1)	(2)	(3)	(4)	(5)	(6)	(7)	(8)
Mrk 33	10 32 31.82	+54 24 02.5	H II	22.9	348 \pm 37.2	91 \pm 5.2	41 \pm 3.2
NGC 24	00 09 56.37	-24 57 51.2	H II	7.3	442 \pm 33.8	67 \pm 3.1	31 \pm 4.6
NGC 337	00 59 50.20	-07 34 45.8	H II	22.4	427 \pm 7.2	69 \pm 0.1	31 \pm 0.2
NGC 628	01 36 41.60	+15 47 00.0	H II	7.3	316 \pm 4.1	65 \pm 2.0	61 \pm 17.6
NGC 855	02 14 03.70	+27 52 38.4	H II	9.6	687 \pm 255.3	67 \pm 1.0	32 \pm 0.9
NGC 925	02 27 17.25	+33 34 41.6	H II	9.1	434 \pm 8.6	65 \pm 0.4	27 \pm 0.6
NGC 1482	03 54 38.88	-20 30 07.1	H II	23.2	455 \pm 1.7	70 \pm 0.2	37 \pm 0.6
NGC 2403	07 36 49.95	+65 36 03.5	H II	3.2	439 \pm 6.3	60 \pm 0.2	25 \pm 0.3
NGC 2798	09 17 22.80	+41 59 59.4	H II	26.2	325 \pm 2.4	87 \pm 0.1	46 \pm 0.1
NGC 2915	09 26 10.03	-76 37 32.2	H II	3.8	371 \pm 7.8	62 \pm 5.8	23 \pm 5.5
NGC 2976	09 47 15.22	+67 55 00.3	H II	3.6	313 \pm 2.8	67 \pm 0.3	27 \pm 0.4
NGC 3049	09 54 49.59	+09 16 18.1	H II	23.9	381 \pm 14.7	85 \pm 0.2	39 \pm 0.2
NGC 3184	10 18 16.90	+41 25 24.7	H II	11.1	354 \pm 7.7	74 \pm 0.3	32 \pm 0.5
NGC 3265	10 31 06.80	+28 47 45.6	H II	23.2	359 \pm 12.5	77 \pm 0.3	38 \pm 0.3
NGC 3351	10 43 57.72	+11 42 13.5	H II	9.3	349 \pm 2.3	82 \pm 0.1	39 \pm 0.1
NGC 3773	11 38 12.98	+12 06 45.8	H II	11.9	366 \pm 14.2	75 \pm 0.5	34 \pm 0.6
NGC 4254	12 18 49.57	+14 24 57.5	H II	16.6	375 \pm 2.7	72 \pm 0.2	35 \pm 0.2
NGC 4536	12 34 27.03	+02 11 16.5	H II	14.4	500 \pm 3.2	69 \pm 0.1	32 \pm 0.1
NGC 4559	12 35 57.58	+27 57 34.2	H II	10.3	386 \pm 9.5	63 \pm 1.8	27 \pm 1.5
NGC 4625	12 41 52.68	+41 16 26.9	H II	9.2	397 \pm 12.0	64 \pm 0.7	26 \pm 3.8
NGC 4631	12 42 07.80	+32 32 34.6	H II	8.1	473 \pm 2.1	66 \pm 0.3	34 \pm 0.6
NGC 5713	14 40 11.38	-00 17 24.2	H II	29.4	435 \pm 3.9	79 \pm 0.1	40 \pm 0.1
NGC 6946	20 34 52.23	+60 09 14.4	H II	6.8	394 \pm 1.5	74 \pm 0.0	39 \pm 0.1
NGC 7793	23 57 49.84	-32 35 27.1	H II	3.8	378 \pm 7.4	68 \pm 0.5	31 \pm 0.6
NGC 1097	02 46 18.86	-30 16 27.2	LINER	17.1	360 \pm 0.5	81 \pm 0.0	41 \pm 0.0
NGC 1266	03 16 00.71	-02 25 36.9	LINER	30.0	213 \pm 3.8	73 \pm 1.0	49 \pm 0.3
NGC 1512	04 03 54.17	-43 20 54.4	LINER	11.8	407 \pm 5.9	76 \pm 0.6	37 \pm 0.5
NGC 1566	04 20 00.33	-54 56 16.6	Seyfert	20.3	337 \pm 1.9	114 \pm 0.3	46 \pm 0.1
NGC 3198	10 19 54.84	+45 32 58.7	LINER	13.7	235 \pm 0.9	107 \pm 5.9	65 \pm 0.1
NGC 3521	11 05 48.58	-00 02 07.3	LINER	10.1	391 \pm 3.4	250 \pm 0.0	57 \pm 0.1
NGC 3621	11 18 16.51	-32 48 49.3	LINER	6.6	426 \pm 4.1	65 \pm 0.2	29 \pm 0.4
NGC 3627	11 20 15.04	+12 59 29.0	Seyfert	9.4	395 \pm 2.3	99 \pm 0.4	45 \pm 0.1
NGC 3938	11 52 49.32	+44 07 13.6	LINER	13.3	314 \pm 1.8	250 \pm 0.0	63 \pm 0.2
NGC 4321	12 22 54.87	+15 49 19.2	LINER	14.3	359 \pm 3.7	74 \pm 0.1	37 \pm 0.1
NGC 4450	12 28 29.71	+17 05 08.7	LINER	16.6	500 \pm 11.7	128 \pm 2.3	40 \pm 1.0
NGC 4569	12 36 49.76	+13 09 45.5	Seyfert	16.6	356 \pm 2.4	101 \pm 0.2	41 \pm 0.1
NGC 4579	12 37 43.53	+11 49 03.8	Seyfert	16.6	361 \pm 3.5	124 \pm 1.0	43 \pm 0.3
NGC 4736	12 50 53.15	+41 07 14.4	LINER	5.0	1500 \pm 0.0	214 \pm 0.2	48 \pm 0.0
NGC 4826	12 56 43.59	+21 40 58.0	Seyfert	5.0	435 \pm 1.2	76 \pm 0.1	38 \pm 0.1
NGC 5033	13 13 27.32	+36 35 35.2	Seyfert	14.8	390 \pm 2.2	88 \pm 0.7	45 \pm 0.2
NGC 5055	13 15 49.35	+42 01 45.7	LINER	7.8	380 \pm 1.6	100 \pm 0.5	45 \pm 0.1
NGC 5194	13 29 52.80	+47 11 43.5	Seyfert	7.8	335 \pm 1.0	84 \pm 0.2	41 \pm 0.1
NGC 5195	13 29 59.50	+47 15 56.7	Seyfert	8.0	422 \pm 2.1	117 \pm 0.4	48 \pm 0.1
NGC 5866	15 06 29.48	+55 45 45.0	LINER	15.1	864 \pm 47.4	193 \pm 3.1	44 \pm 0.2
NGC 7331	22 37 04.15	+34 24 55.3	LINER	14.5	467 \pm 4.7	131 \pm 1.5	48 \pm 0.2
NGC 7552	23 16 10.83	-42 35 05.5	LINER	21.0	339 \pm 1.1	91 \pm 0.1	48 \pm 0.1
DCld 300.2-16.9 (A)	11 54 23.10	-79 31 42.0	HLC	70 \pm 15E-6	500 \pm 6.9	102 \pm 0.5	45 \pm 0.4
DCld 300.2-16.9 (B)	11 52 08.30	-79 09 33.0	HLC	70 \pm 15E-6	460 \pm 3.6	84 \pm 0.6	45 \pm 0.6
DCld 300.2-16.9 (C)	11 48 24.40	-79 18 00.0	HLC	70 \pm 15E-6	371 \pm 2.4	95 \pm 0.5	45 \pm 0.5
DCld 300.2-16.9 (D)	11 55 33.80	-79 20 54.0	HLC	70 \pm 15E-6	394 \pm 4.1	106 \pm 0.6	48 \pm 0.4

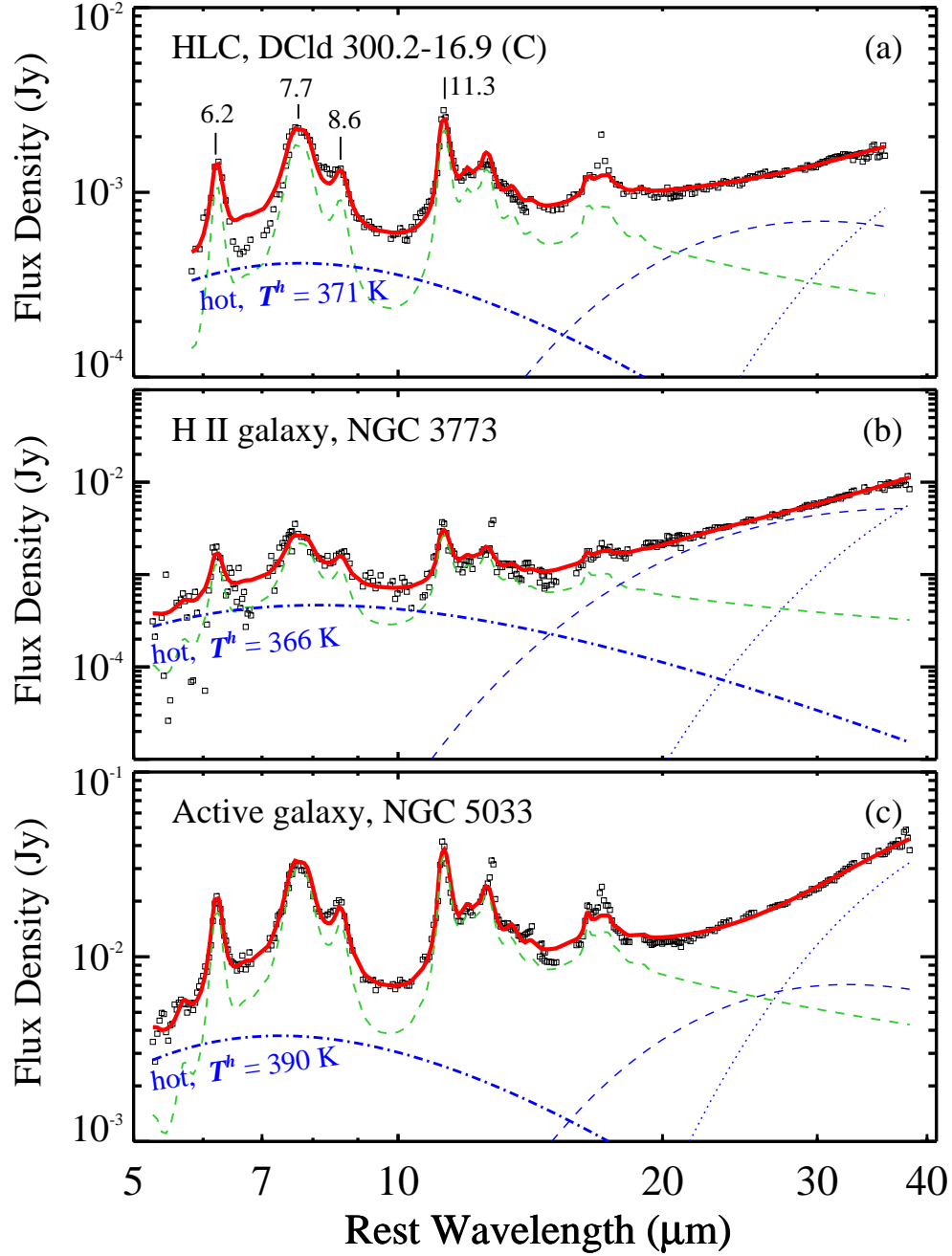


Fig. 1.— Spectral decomposition of the MIR spectra of (a) HLC DC1d 300.2-16.9 (C), (b) the H II galaxy NGC 3773, and (c) the Seyfert galaxy NGC 5033. Each panel shows the observed *Spitzer*/IRS spectrum (black squares) and the best-fit model (solid red line), comprising a theoretical PAH template (green dashed line; main PAH features labeled in top panel) and three dust components (hot: blue dot-dashed line; warm: blue dashed line; cold: blue dotted line). The temperature of the hot component is labeled. The main PAH emission features at 6.2, 7.7, 8.6 and 11.3 μm are also labeled in the top panel.

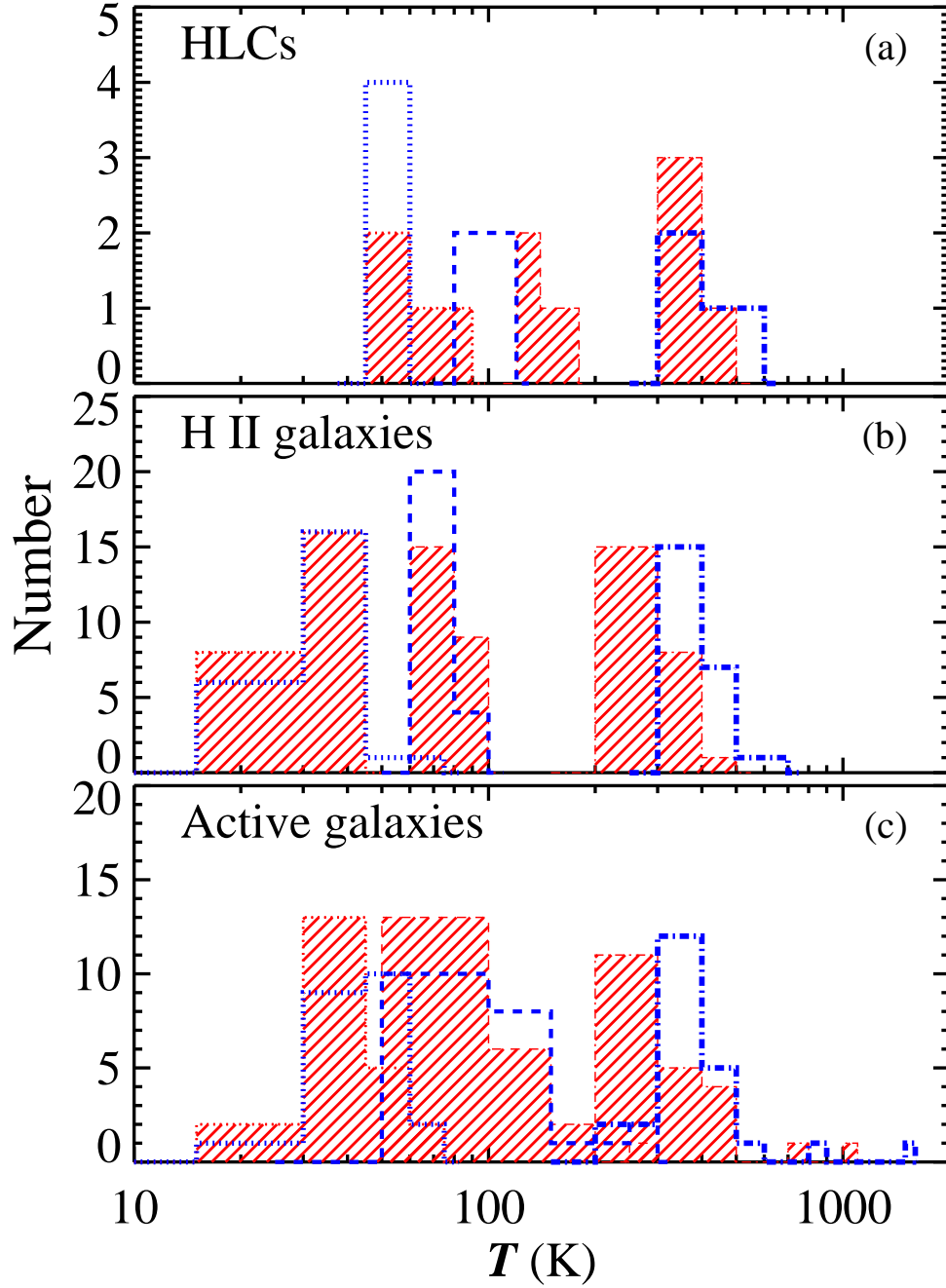


Fig. 2.— Temperature distributions of the three dust components. The one derived based on theoretical PAH template are plotted in blue color (hot: dot-dashed line; warm: dashed line; cold: dotted line) for (a) HLCs, (b) H II galaxies, and (c) active (LINER and Seyfert) galaxies. The one derived based on an alternate empirical PAH template (CAFE; Marshall et al. 2007) are in red shaded area wrapped with different lines (hot: dot-dashed line; warm: dashed line; cold: dotted line) for (a) HLCs, (b) H II galaxies, and (c) active (LINER and Seyfert) galaxies.

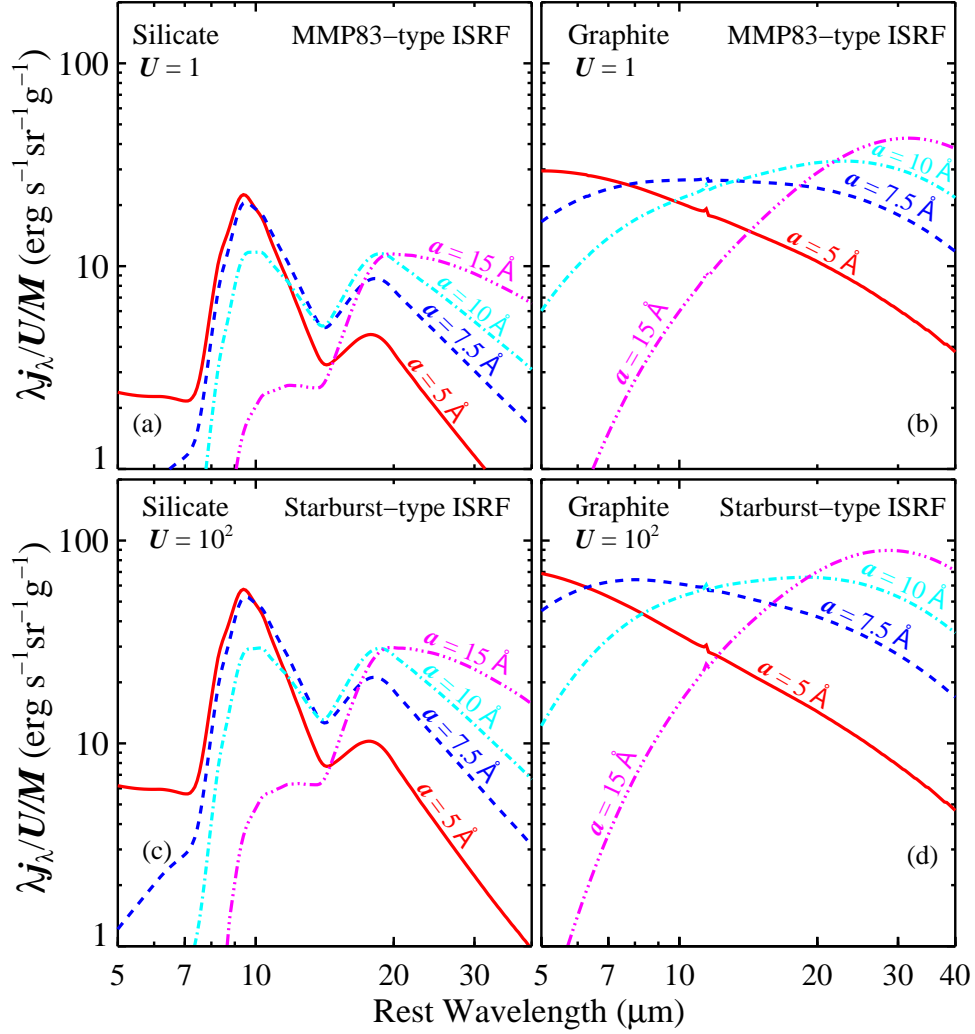


Fig. 3.— IR emissivity (normalized by dust mass M and starlight intensity U) for single-size silicate (a, c) and graphite (b, d) grains of $a = 5 \text{ \AA}$ (red solid line), $a = 7.5 \text{ \AA}$ (blue dashed line), $a = 10 \text{ \AA}$ (cyan dot-dashed line), and $a = 15 \text{ \AA}$ (magenta dot-dot-dashed line) illuminated by the MMP83-type ISRF of $U = 1$ (a, b) and the starburst-type ISRF of $U = 100$ (c, d).

Table 2. *Herschel* Photometry of GOALS Galaxies Used in Our Analysis

Source	Redshift	$\log(\frac{L_{\text{IR}}}{L_{\odot}})$	F_{70}	F_{100}	F_{160}	F_{250}	F_{350}	F_{500}
(1)	(2)	(3)	(Jy)	(Jy)	(Jy)	(Jy)	(Jy)	(Jy)
ESO 286-G035	0.01736	11.20	9.50±0.44	12.80±0.58	10.40±0.47	3.99±0.24	1.47±0.09	0.40±0.03
ESO 319-G022	0.01635	11.12	9.09±0.41	10.50±0.48	7.79±0.34	3.09±0.19	1.14±0.07	0.32±0.02
ESO 353-G020	0.01600	11.06	10.60±0.49	16.40±0.75	15.30±0.68	6.57±0.41	2.62±0.16	0.88±0.06
ESO 557-G002	0.02130	11.25	8.70±0.34	10.30±0.38	7.69±0.28	3.01±0.14	1.16±0.06	0.35±0.02
IC 0860	0.01116	11.14	19.70±0.90	18.10±0.82	10.70±0.47	3.78±0.23	1.52±0.09	0.50±0.03
IC 2810	0.03400	11.64	8.46±0.28	11.40±0.38	9.35±0.30	3.82±0.25	1.61±0.11	0.54±0.04
IC 4734	0.01561	11.35	19.10±0.88	25.40±1.16	20.50±0.92	8.45±0.53	3.26±0.20	1.05±0.07
IRAS F01364-1042	0.04825	11.85	7.40±0.33	6.85±0.31	3.99±0.17	1.34±0.08	0.52±0.03	0.16±0.01
IRAS F03514+1546	0.02222	11.20	6.67±0.33	8.85±0.44	6.95±0.35	3.07±0.19	1.13±0.07	0.36±0.03
IRAS F06076-2139	0.03745	11.65	7.55±0.34	8.41±0.37	5.66±0.24	2.16±0.13	0.86±0.05	0.27±0.02
IRAS F06592-6313	0.02296	11.24	6.90±0.31	7.53±0.34	5.03±0.22	1.84±0.11	0.76±0.05	0.22±0.02
IRAS F10565+2448	0.04310	12.08	14.30±0.64	15.80±0.71	10.50±0.46	3.64±0.22	1.34±0.08	0.38±0.02
IRAS F14179+4927	0.02574	11.39	6.51±0.33	7.45±0.37	4.90±0.25	1.79±0.12	0.69±0.05	0.18±0.02
IRAS F16284+0411	0.02449	11.45	9.15±0.41	12.50±0.55	10.00±0.44	3.62±0.24	1.42±0.10	0.49±0.04
IRAS F17132+5313	0.05094	11.96	6.21±0.31	6.98±0.35	5.47±0.24	2.01±0.12	0.78±0.05	0.23±0.02
IRAS F17207-0014	0.04281	12.46	38.10±1.74	37.90±1.72	23.10±1.02	7.96±0.49	2.91±0.18	0.89±0.05
IRAS F18293-3413	0.01818	11.88	45.70±2.11	59.10±2.71	45.80±2.07	17.20±1.07	6.45±0.40	1.99±0.12
IRAS F22491-1808	0.07776	12.20	5.64±0.25	4.98±0.22	2.72±0.12	0.84±0.05	0.31±0.02	0.08±0.01
MCG 02-04-025	0.03123	11.69	11.70±0.53	11.30±0.51	6.91±0.31	2.13±0.13	0.77±0.05	0.23±0.02
MCG 02-20-003	0.01625	11.13	10.60±0.48	13.10±0.59	9.97±0.44	4.07±0.25	1.56±0.10	0.50±0.03
MCG 03-04-014	0.03349	11.65	9.00±0.41	11.40±0.51	8.76±0.39	3.08±0.19	1.18±0.07	0.35±0.02
MCG 05-12-006	0.01875	11.17	9.17±0.41	10.40±0.46	6.95±0.30	2.45±0.15	0.91±0.06	0.27±0.02
UGC 01385	0.01875	11.05	6.77±0.30	8.27±0.36	6.29±0.25	2.54±0.13	1.03±0.06	0.28±0.03
UGC 01845	0.01561	11.12	13.10±0.59	17.50±0.78	13.80±0.60	5.04±0.30	1.97±0.12	0.56±0.03
UGC 12150	0.02139	11.35	10.70±0.48	14.70±0.66	12.30±0.54	5.09±0.31	2.03±0.12	0.61±0.04
VII Zw 031	0.05367	11.99	7.49±0.34	10.10±0.45	8.06±0.35	3.13±0.19	1.17±0.07	0.35±0.02
VV 250a	0.03107	11.81	11.70±0.59	11.20±0.56	6.73±0.34	2.43±0.16	0.88±0.06	0.27±0.02
UGC 03608	0.02135	11.33	8.88±0.44	10.60±0.53	8.32±0.42	3.59±0.22	1.36±0.08	0.43±0.03

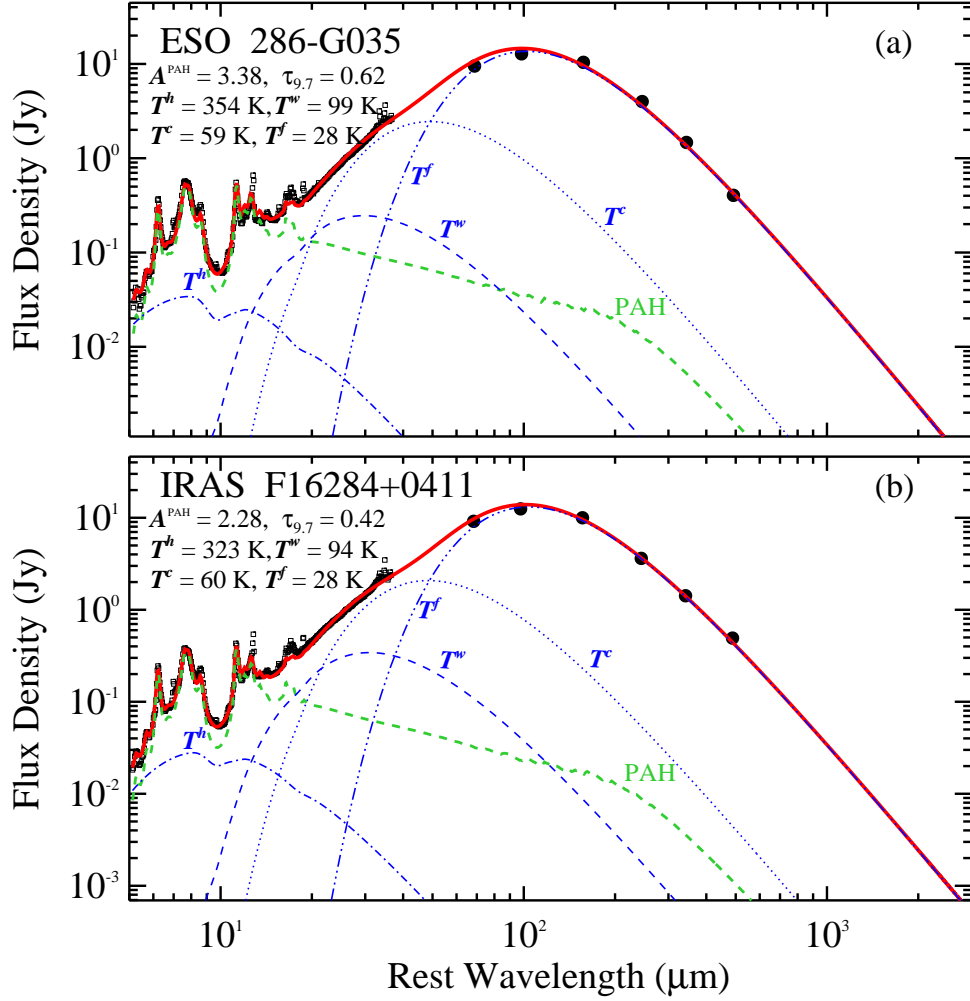


Fig. 4.— Decomposition of the SED of (a) ESO 286-G035 and (b) IRAS F16284+0411. The SED is extended to the far-IR using photometric measurements from *Herschel* at 70, 100, 160, 250, 350, and $500 \mu\text{m}$. Each panel shows the observed *Spitzer*/IRS spectrum (black squares), far-IR photometry (black filled circles), and the best-fit model (solid red line), comprising a theoretical PAH template (green dashed line) and four dust components (hot: blue dot-dashed line; warm: blue dashed line; cold: blue dotted line; extreme cold: blue dot-dot-dotted line).

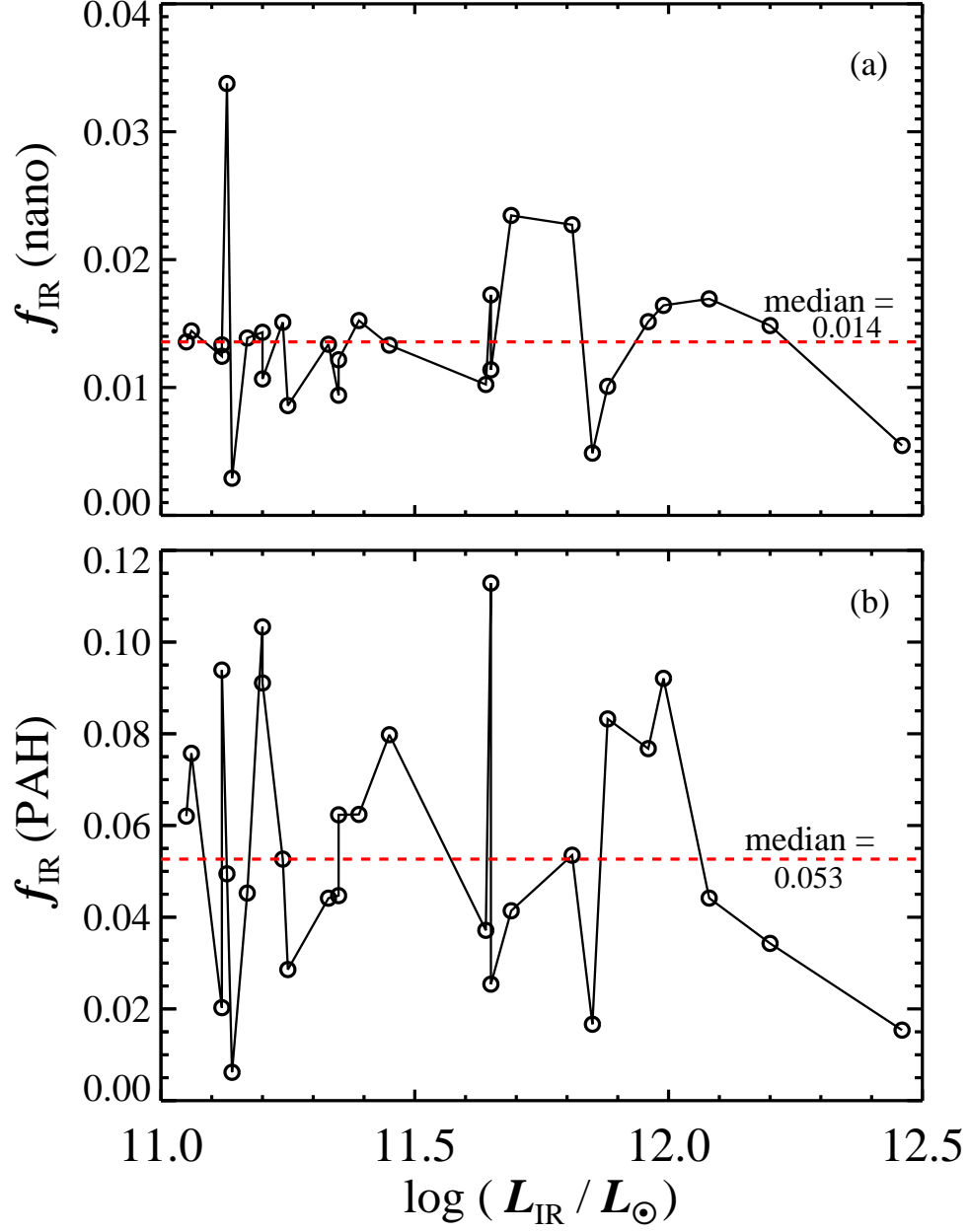


Fig. 5.— The fraction of the total IR power emitted by (a) the nano dust component and (b) PAHs.

REFERENCES

- Allamandola, L. J., Tielens, A. G. G. M., & Barker, J. R. 1985, *ApJ*, 290, L25
- An, J. H., & Sellgren, K. 2003, *ApJ*, 599, 312
- Andersson, O. E., Prasad, B. L. V., Sato, H., et al. 1998, *Phys. Rev. B*, 58, 16387
- Andriesse, C. D. 1978, *A&A*, 66, 169
- Andriesse, C. D., & de Vries, J. S. 1976, *A&A*, 46, 143
- Arendt, R. G., Odegard, N., Weiland, J. L., et al. 1998, *ApJ*, 508, 74
- Armus, L., Charmandaris, V., Bernard-Salas, J., et al. 2007, *ApJ*, 656, 148
- Armus, L., Mazzarella, J. M., Evans, A. S., et al. 2009, *PASP*, 121, 559
- Auld, R., Bianchi, S., Smith, M. W. L., et al. 2013, *MNRAS*, 428, 1880
- Bauschlicher, C. W., Jr., Ricca, A., Boersma, C., & Allamandola, L. J. 2018, *ApJS*, 234, 32
- Brown, M. J. I., Moustakas, J., Smith, J.-D. T., et al. 2014, *ApJS*, 212, 18
- Boissel, P., Joblin, C., & Pernot, P. 2001, *A&A*, 373, L5
- Boulanger, F., & Péroult, M. 1988, *ApJ*, 330, 964
- Boulanger, F., Abergel, A., Cesarsky, D., et al. 2000, *ISO Beyond Point Sources: Studies of Extended Infrared Emission*, 455, 91
- Chu, J. K., Sanders, D. B., Larson, K. L., et al. 2017, *ApJS*, 229, 25
- Compiègne, M., Verstraete, L., Jones, A., et al. 2011, *A&A*, 525, A103
- Dale, D. A., Aniano, G., Engelbracht, C. W., et al. 2012, *ApJ*, 745, 95
- Désert, F.-X., Boulanger, F., & Puget, J. L. 1990, *A&A*, 237, 215
- Draine, B. T. 1988, *ApJ*, 333, 848
- Draine B.T. 1989, in *IAU Symp. 135, Interstellar Dust*, ed L. J. Allamandola & A. G. G. M. Tielens (Dordrecht: Kluwer), 313
- Draine, B. T. 2003, *ARA&A*, 41, 241
- Draine, B. T., & Anderson, N. 1985, *ApJ*, 292, 494

- Draine, B. T., & Lazarian, A. 1998, *ApJ*, 508, 157
- Draine, B. T., & Li, A. 2001, *ApJ*, 551, 807
- Draine, B. T., & Li, A. 2007, *ApJ*, 657, 810
- Duley, W. W. 1973, *Ap&SS*, 23, 43
- Dunne, L., Gomez, H. L., da Cunha, E., et al. 2011, *MNRAS*, 417, 1510
- Dwek, E., Arendt, R. G., Fixsen, D. J., et al. 1997, *ApJ*, 475, 565
- Greenberg, J. M. 1968, in *Stars and Stellar Systems*, Vol. 7, ed. B. M. Middlehurst & L. H. Aller (Chicago : Univ. Chicago Press), 221
- Greenberg, J. M., & Hong, S.-S. 1974, in *IAU Symp. 60: Galactic Radio Astronomy* (Dordrecht: Reide), 155
- Helou, G., Lu, N. Y., Werner, M. W., Malhotra, S., & Silbermann, N. 2000, *ApJ*, 532, L21
- Hensley, B. S., & Draine, B. T. 2017a, *ApJ*, 836, 179
- Hensley, B. S., & Draine, B. T. 2017b, *ApJ*, 834, 134
- Ho, L. C. 2008, *ARA&A*, 46, 475
- Ho, L. C. 2009, *ApJ*, 699, 626
- Henning, T., & Mutschke, H. 1997, *A&A*, 327, 743
- Houck, J. R., Roellig, T. L., van Cleve, J., et al. 2004, *ApJS*, 154, 18
- Ingalls, J. G., Bania, T. M., Boulanger, F., et al. 2011, *ApJ*, 743, 174
- Jones, A. P. 1990, *MNRAS*, 245, 331
- Kahanpää, J., Mattila, K., Lehtinen, K., Leinert, C., & Lemke, D. 2003, *A&A*, 405, 999
- Kennicutt Jr., R. C., Armus, L., Bendo, G., et al. 2003, *PASP*, 115, 928
- Koike, C., Matsuno, J., & Chihara, H. 2017, *ApJ*, 845, 115
- Kwok, S., & Zhang, Y. 2011, *Nature*, 479, 80
- Léger, A., & Puget, J. L. 1984, *A&A*, 137, L5
- Lewis, R. S., Ming, T., Wacker, J. F., Anders, E., & Steel, E. 1987, *Nature*, 326, 160

- Li, A. 2004a, in *Astrophysics of Dust* (ASP Conf. Ser. 309), ed. A. N. Witt, G. C. Clayton, & B. T. Draine (San Francisco, CA: ASP), 417
- Li, A. 2004b, in *Penetrating Bars Through Masks of Cosmic Dust*, ed. D.L. Block et al. (Dordrecht: Springer), 535 (astro-ph/0503571)
- Li, A. 2009, in *Small Bodies in Planetary Sciences* (Lecture Notes in Physics Vol. 758), ed. I. Mann, A. Nakamura, & T. Mukai (Springer), 167
- Li, A., & Draine, B. T. 2001, *ApJ*, 554, 778
- Li, A., & Greenberg, J. M. 1997, *A&A*, 323, 566
- Licquia, T. C., Newman, J. A., & Brinchmann, J. 2015, *ApJ*, 809, 96
- Lu, N., Helou, G., Werner, M. W., et al. 2003, *ApJ*, 588, 199
- Markwardt, C. B. 2009, *Astronomical Data Analysis Software and Systems XVIII*, 411, 251
- Marshall, J. A., Herter, T. L., Armus, L., et al. 2007, *ApJ*, 670, 129
- Mathis, J. S., Mezger, P. G., & Panagia, N. 1983, *A&A*, 128, 212
- Mishra, A., & Li, A. 2015, *ApJ*, 809, 120
- Mishra, A., & Li, A. 2017, *ApJ*, 850, 138
- Pendleton, Y. J., & Allamandola, L. J. 2002, *ApJS*, 138, 75
- Planck Collaboration, Abergel, A., Ade, P. A. R., et al. 2011, *A&A*, 536, A21
- Platt, J. R. 1956, *ApJ*, 123, 486
- Purcell, E. M. 1976, *ApJ*, 206, 685
- Rapacioli, M., Joblin, C., & Boissel, P. 2005, *A&A*, 429, 193
- Sanders, D. B., Mazzarella, J. M., Kim, D.-C., Surace, J. A., & Soifer, B. T. 2003, *AJ*, 126, 1607
- Scoville, N., Aussel, H., Sheth, K., et al. 2014, *ApJ*, 783, 84
- Sellgren, K., Werner, M. W., & Dinerstein, H. L. 1983, *ApJ*, 271, L13
- Sellgren, K. 1984, *ApJ*, 277, 623

- Siebenmorgen, R., & Kruegel, E. 1992, *A&A*, 259, 614
- Smith, J. D. T., Draine, B. T., Dale, D. A., et al. 2007, *ApJ*, 656, 770
- Stecher, T. P., & Donn, B. 1965, *ApJ*, 142, 1681
- Sturm, E., Lutz, D., Tran, D., et al. 2000, *A&A*, 358, 481
- Wang, S., Li, A., & Jiang, B. W. 2015, *ApJ*, 811, 38
- Weiland, J. L., Blitz, L., Dwek, E., et al. 1986, *ApJ*, 306, L101
- Werner, M. W., Roellig, T. L., Low, F. J., et al. 2004, *ApJS*, 154, 1
- Weingartner, J. C., & Draine, B. T. 2001, *ApJ*, 548, 296
- Witt, A. N. 2000, *J. Geophys. Res.*, 105, 10299
- Xie, Y., Ho, L. C., Li, A., & Shangguan, J. 2018, *ApJ*, 860, 154
- Xie, Y., Li, A., & Hao, L. 2017, *ApJS*, 228, 6
- Yang, X. J., Glaser, R., Li, A., & Zhong, J. X. 2013, *ApJ*, 776, 110
- Zhuang, M.-Y., Ho, L. C., & Shangguan, J. 2018, *ApJ*, 862, 118
- Zubko, V., Dwek, E., & Arendt, R. G. 2004, *ApJS*, 152, 211